Evolution of Compensated Magnetism and Spin-Torque Switching in Ferrimagnetic $Fe_{1-x}Tb_x$

Teng Xu,[1,2,†] Yang Cheng,[1,2,†] Yiqing Dong,[1,2,†] Hao Bai,[1,2] Heng-An Zhou,[1,2] Xinyu Shu,[1,2] Pierluigi Gargiani,[4] Manuel Valvidares,[4] Pu Yu,[1,2,3] and Wanjun Jiang[1,2,3,*]

[1] *State Key Laboratory of Low-Dimensional Quantum Physics and Department of Physics, Tsinghua University, Beijing 100084, China*

[2] *Frontier Science Center for Quantum Information, Tsinghua University, Beijing 100084, China*

[3] *Collaborative Innovation Center of Quantum Matter, Beijing 100084, China*

[4] *ALBA Synchrotron Light Source, Cerdanyola del Vallès, 08290 Barcelona, Spain*

(Received 13 October 2022; revised 16 January 2023; accepted 23 February 2023; published 27 March 2023)

Compensated ferrimagnets (FIMs) made of rare-earth transition-metal compounds have stimulated increasing interest for enabling fast spin dynamics. Taking Fe-Tb compounds as an example, substantial efforts have been made on the study of compensated magnetism and its potential spintronic applications. Current-induced spin-orbit torque (SOT) switching and its evolution with compensated ferrimagnetism in these compounds, however, remain to be systematically explored, which motivates the present study. By combining magnetometry and anomalous Hall effect measurements, a compositional magnetization compensation point ($x_c = 0.25$) is determined for $Fe_{1-x}Tb_x$ films of a fixed thickness of 6.5 nm. The antiferromagnetic coupling between Fe and Tb sublattices is directly revealed by conducting element-specific x-ray magnetic circular dichroism measurements. The evolution of SOT switching as a function of Tb concentration (x) in $Pt/Fe_{1-x}Tb_x/Ta$ multilayers is subsequently investigated. An enhanced SOT efficiency (approximately 3 times) is obtained at $x_c = 0.25$. By conducting an endurance test, reliable SOT switching is revealed for over 10^4 cycles. Our work suggests that compensated FIMs of composition $Fe_{1-x}Tb_x$ could be implemented for realizing efficient and stable spin-orbitronic performances.

DOI: 10.1103/PhysRevApplied.19.034088

I. INTRODUCTION

Compensated ferrimagnets (FIMs) with bulk perpendicular magnetic anisotropy (PMA) have attracted growing attention from the spintronic community, due to their potential applications in high-density, high-speed, and high-efficiency spin-orbitronic devices [1–5]. Typical FIMs are made of two or more inequivalent and antiparallel sublattices, which lead to antiferromagnet (AFM)-like spin dynamics [6–8]. In contrast to standard AFMs, a finite net magnetization remains in FIMs, as a result of the uncompensated moments from sublattices, which can be easily manipulated and detected [9–15]. Along this direction, significant progress has been made, including efficient magnetization switching [9,10,16], ultrafast current-driven domain wall motion [17–21], and the realization of nanoscale ferrimagnetic skyrmions [22–25]. There progresses were made typically through utilizing current-induced spin-orbit torques (SOTs) by interfacing compensated FIMs with heavy metals (HMs), which exhibit strong spin-orbit couplings [26–30]. The involved compensated FIMs of composition Gd-Fe-Co and Co-Gd [9,12,16,31] generally possess a relatively weak PMA and hence a weak magnetic anisotropy energy (K_u). In this work, we study the evolution of SOT switching and its connection with compensated magnetism in $Fe_{1-x}Tb_x$ films, which exhibit a rather strong PMA and an enhanced K_u.

This paper is organized as follows. (1) Magnetometry together with anomalous Hall effect (AHE) measurements are conducted to determine the compensated magnetism in $Fe_{1-x}Tb_x$ films. (2) The onset of AFM coupling is identified using the element-specific x-ray magnetic circular dichroism (XMCD) technique. (3) Current-induced SOTs are utilized to switch the magnetization. (4) Harmonic Hall measurements are employed to identify the SOT efficiency, revealing an enhanced SOT efficiency when fully compensated magnetism occurs. (5) An endurance test is made by repeating SOT switching for over 10^4 cycles. Our results demonstrate that the $Fe_{1-x}Tb_x$ compensated FIMs could provide a promising platform for spin-orbitronic devices, while exhibiting high efficiency and stability.

*jiang_lab@tsinghua.edu.cn

†These authors contributed equally to this work.

II. MATERIALS AND METHODS

Magnetic multilayers of stacking order Ta(1)/Pt(3)/$Fe_{1-x}Tb_x$(6.5)/Ta(3)/Si_3N_4(5) (numbers denote the thickness in nanometers) are fabricated on thermally oxidized silicon substrates using an ultrahigh-vacuum magnetron sputtering system. The base pressure of the main chamber is better than 1×10^{-8} Torr and the Ar pressure is 3 mTorr. A 1 nm Ta layer is used as an adhesive layer and a Si_3N_4 (5 nm) layer is used for preventing oxidization. Note that the Si_3N_4 layer is deposited through using a compound Si_3N_4 sputtering target. The amorphous $Fe_{1-x}Tb_x$ layers are synthesized by co-sputtering Fe and Tb targets, in which Tb concentration (x) can be adjusted by fixing the growth power of Fe target while changing the growth power of Tb target. No detectable segregation of Fe and Tb elements is observed in a high-resolution transmission electron microscopy experiment [32].

Magnetic properties of films are characterized using a superconducting quantum interference device and vibrating sample magnetometry. The AHE measurements are performed using a home-built electrical transport measurement system. Magnetic multilayers are patterned into standard Hall bar devices with a channel width of 20 μm utilizing standard photolithography and Ar ion milling. Current-induced magnetization switching is performed by injecting current pulses of duration of 2 ms into the Hall bar device and the corresponding AHE resistances are detected using a lock-in amplifier (SR830). A low-frequency alternating-current (ac) harmonic measurement using the lock-in technique is employed and two lock-in amplifiers are used to simultaneously record the first-harmonic ($V_{1\omega}$) and second-harmonic ($V_{2\omega}$) signals. Element-specific x-ray absorption spectroscopy and XMCD magnetometry measurements are conducted at the Fe $L_{2,3}$ and the Tb $M_{4,5}$ edges at the BOREAS beamline of ALBA Synchrotron Light Source [33]. In the XMCD measurements, magnetic fields are applied collinearly along the incoming x-ray direction and normal to the sample plane, which is sensitive to the perpendicular magnetization component.

III. RESULTS AND DISCUSSION

A. Compensated magnetism in $Fe_{1-x}Tb_x$ ferrimagnet

Figure 1(a) shows the perpendicular magnetic hysteresis loops (M–H_z) of Pt/$Fe_{1-x}Tb_x$/Ta multilayers, in which Tb concentration (x) is changed from $x = 0.18$ to $x = 0.37$. The observed square loops confirm the presence of PMA. Due to the AFM coupling between the Tb ($\boldsymbol{m}_{\mathrm{Tb}}$) and Fe ($\boldsymbol{m}_{\mathrm{Fe}}$) elements [see the inset of Fig. 1(a)], an increased Tb concentration (x) leads to a reduced net saturation magnetization M_S, which reaches a minimum around $x = 0.25$, as shown in the top panel of Fig. 1(b). A further increase of Tb concentration leads to a maximized $M_S \sim 282$ emu/cm^3 at $x = 0.37$. When $x > 0.37$, the absence of PMA occurs, which is irrelevant to this study.

The anisotropy field (H_K) is determined from planar Hall effect (PHE) measurements, which increases to approximately 9 T at $x = 0.27$, as shown in the top panel of Fig. 1(b). The PHE loops can be found in part 1 of the Supplemental Material [34]. For comparison, the magnetic anisotropy energy constants $K_u(= (1/2)M_sH_K)$ of typical rare earth (RE)-transition metal (TM) FIMs are summarized in Table I of the Supplemental Material [34]. It can be seen that $Fe_{1-x}Tb_x$ films possess larger K_u, as compared with other RE-TM FIMs [9,12,16,35]. The evolution of coercive field H_C as a function of Tb concentration (x) is shown in the bottom panel of Fig. 1(b), which reaches its maximum at $x = 0.25$. Thus, a compositional compensation point at $x_c = 0.25$ can be determined, at which the magnetic moments of Fe ($\boldsymbol{m}_{\mathrm{Fe}}$) and Tb ($\boldsymbol{m}_{\mathrm{Tb}}$) sublattices are fully compensated. Below x_c ($x < 0.25$), magnetic properties are Fe-dominated, in which the net magnetization orientation ($\boldsymbol{m}_{\mathrm{FeTb}}$) is along Fe sublattice ($\boldsymbol{m}_{\mathrm{Fe}}$) and antiparallel to Tb sublattice ($\boldsymbol{m}_{\mathrm{Tb}}$). Above x_c ($x > 0.25$), magnetic properties are Tb-dominated, in which the net magnetization orientation ($\boldsymbol{m}_{\mathrm{FeTb}}$) is along Tb sublattice ($\boldsymbol{m}_{\mathrm{Tb}}$) and antiparallel to Fe sublattice ($\boldsymbol{m}_{\mathrm{Fe}}$). Note that a compositional compensation point $x_c = 0.47$ has been determined in 20-nm-thick $Fe_{1-x}Tb_x$ single layers [32]. This can be attributed to the thickness-dependent magnetic properties of Fe-Tb, which has been suggested in earlier studies [15].

The results of AHE measurement are shown in Fig. 1(c). The polarity of the AHE loops reverses its sign at the opposite sides of $x_c = 0.25$, which is similar to the case of $Co_{1-x}Gd_x$ and $Co_{1-x}Tb_x$ films [9–12]. This can be explained by the dominance of spin-dependent transport properties from the outer shell $3d$ magnetism of Fe sublattice, as compared with the inner shell $4f$ magnetism of Tb element [36–38]. This also explains the sign reversal of the AHE resistances between the Fe-dominated ($x = 0.18$–0.25) and the Tb-dominated ($x = 0.25$–0.37) samples, as shown in Fig. 1(d). Note that the amplitude of the AHE resistance ($|\Delta R_{xy}|$) shows a monotonic decrease following the increase of Tb concentration (x), implying a monotonic reduction of the magnetization of Fe sublattice.

The element-specific XMCD measurement probes directly the relative changes of perpendicular magnetization of Fe (m^z_{Fe}) and Tb (m^z_{Tb}) elements. The XMCD hysteresis loops for $Fe_{0.76}Tb_{0.24}$ and $Fe_{0.68}Tb_{0.32}$ films are shown in Figs. 2(a) and 2(b), respectively. In both samples, the switching polarity of Fe element (m^z_{Fe}–H_z) is opposite to that of Tb element (m^z_{Tb}–H_z), which confirms the AFM coupling between Fe and Tb elements. Moreover, the switching polarity of Fe element in the $Fe_{0.68}Tb_{0.32}$ film is opposite to that of Fe element in the $Fe_{0.76}Tb_{0.24}$ film, which is consistent with the reversed sign of the AHE loops across x_c, as shown in Fig. 1(c). Thus, AFM

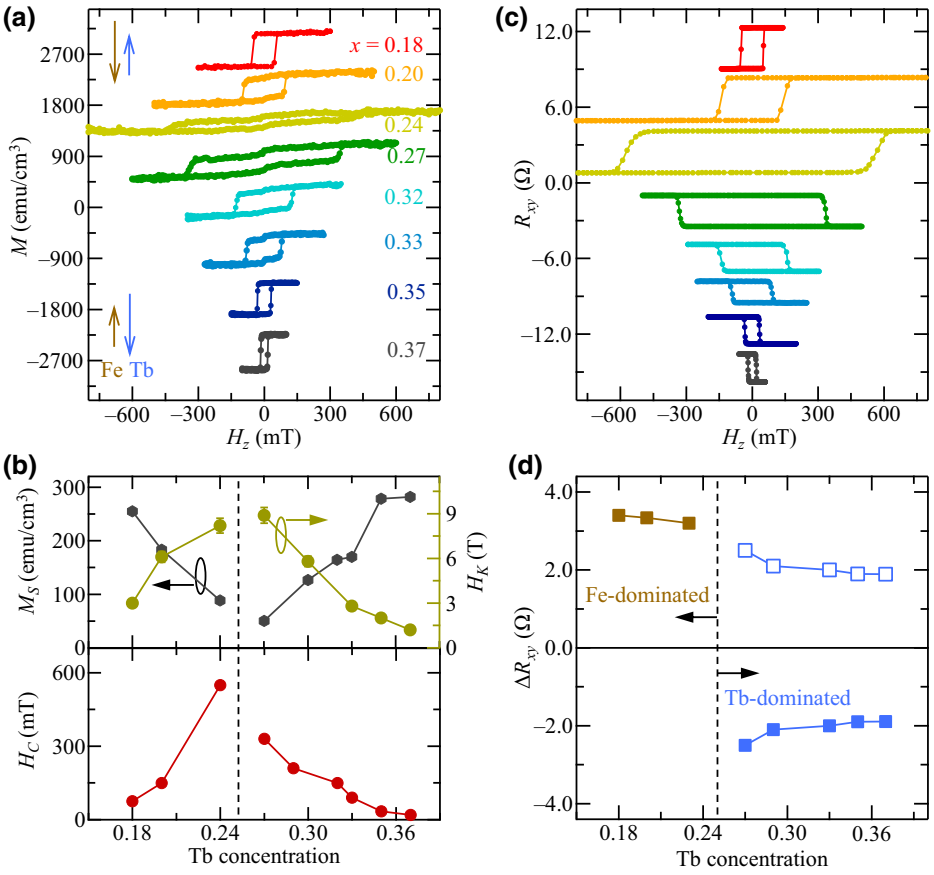

FIG. 1. (a) Magnetic hysteresis loops of $Pt/Fe_{1-x}Tb_x/Ta$ multilayers with increasing Tb concentration (x). The brown and blue arrows denote the magnetization orientations of Fe and Tb sublattices, respectively. (b) The evolution of the net saturation magnetization M_S, the magnetic anisotropy field H_K, and coercive field H_C as a function of Tb concentration (x). (c) The corresponding AHE loops. (d) The AHE resistance difference ΔR_{xy} as a function of Tb concentration (x). The compositional compensation point $x_c = 0.25$ is marked as the dashed line.

coupling between Fe and Tb elements, together with their sign reversal across the compositional compensation point ($x_c = 0.25$), are observed in $Fe_{0.76}Tb_{0.24}$ (Fe-dominated) and $Fe_{0.68}Tb_{0.32}$ (Tb-dominated) films.

B. Spin-torque switching of compensated $Fe_{1-x}Tb_x$ ferrimagnets

In a $Pt/Fe_{1-x}Tb_x/Ta$ multilayer, the bottom Pt and the top Ta layers, which exhibit opposite spin Hall angles [28,29,39,40], can afford complementary SOTs, as schematically shown in Fig. 3(a). An optical image of the Hall bar device is given in Fig. 3(b). During the SOT switching measurements, varied amplitudes of current pulses, but with a fixed duration of 2 ms, are applied. Simultaneously, a longitudinal in-plane magnetic field (H_x) is applied along the current direction (the x axis). Between two consecutive pulses, the magnetization states can be inferred from the AHE resistance (R_{xy}). Current densities flowing in HMs (J_C) are estimated based on a parallel resistor model.

Under $H_x = \pm 100$ mT, the polarity of the SOT switching reverses its sign, as shown in Fig. 3(c). Meanwhile, under the same direction of H_x, the switching polarities reverse their signs across the compositional compensation point (x_c). To qualitatively verify the dominant role of interfacial SOT, inverted multilayers, $Ta/Fe_{0.76}Tb_{0.24}/Pt$ (Fe-dominated) and $Ta/Fe_{0.65}Tb_{0.35}/Pt$ (Tb-dominated), are examined. In these inverted multilayers, SOT switching is from the opposite spin polarization ($-\boldsymbol{\sigma}$) of Ta and Pt layers, which should result in an opposite direction of dampinglike effective field ($\boldsymbol{H}_{\mathrm{DL}} \sim -\boldsymbol{\sigma} \times \boldsymbol{m}_{\mathrm{FeTb}}$). In this case, an opposite polarity of SOT switching is observed, which strongly suggests the dominant role of interfacial SOTs, as shown in part 3 of the Supplemental Material [34].

A control sample of stacking order $SiO_2/Fe_{0.63}Tb_{0.37}/Si_3N_4$ is also studied, which exhibits no switching events with current density up to 10^8 A cm^{-2} (see part 4 of the Supplemental Material [34]). This affirmatively excludes the appreciable contribution of bulk self-torque in Fe-Tb single layer, which has been frequently identified

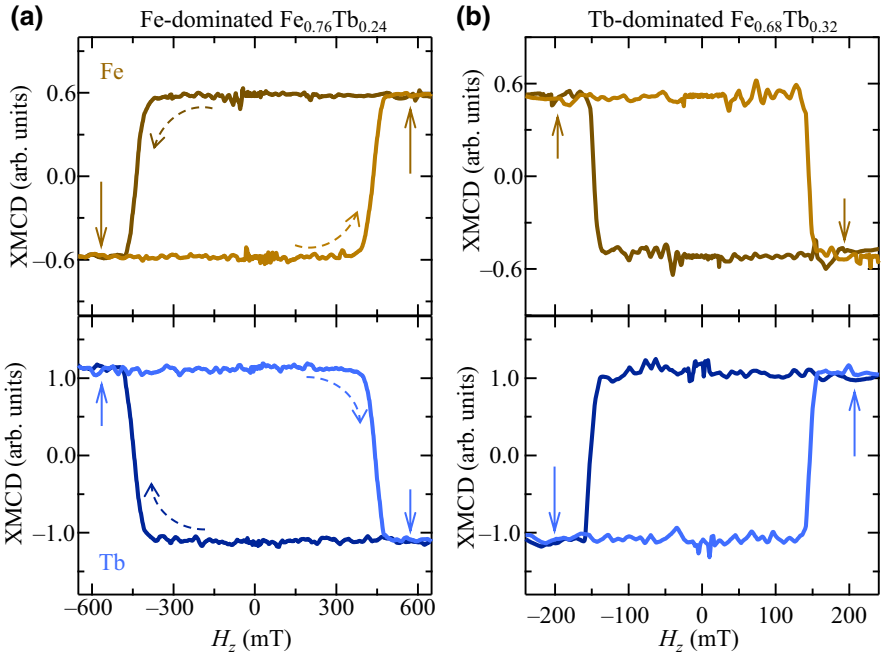

FIG. 2. XMCD hysteresis loops of Fe and Tb elements in Fe-dominated $Fe_{0.76}Tb_{0.24}$ (a) and Tb-dominated $Fe_{0.68}Tb_{0.32}$ (b). The brown and blue arrows denote the magnetization orientations of Fe and Tb sublattices, respectively.

in RE-TM compounds [32,41–43]. For the thin (6.5 nm) $Fe_{1-x}Tb_x$ layers in the present work, the bulk self-torque can be quite weak, as compared with interfacial SOT associated with Pt and Ta layers. Note that Zhu *et al*. have also suggested a negligible bulk self-torque in single-layer $Fe_{1-x}Tb_x$ of thickness of 8 nm [44].

Near the compositional compensation point (x_c), an anomalous switching behavior is observed in the Tb-dominated samples ($x = 0.27$, 0.32). Specifically, the field-driven AHE loop exhibits a Tb-dominated feature, whereas the SOT switching exhibits characteristics as those of the Fe-dominated films. This anomalous SOT switching phenomenon can be attributed to the current-induced Joule heating that raises the device temperature during the switching measurement [9,45]. This can also be understood by invoking the characteristic magnetization compensation temperature (T_M) in RE-TM compounds. Below and above T_M, the dominant magnetization is from either the RE or TM sublattices, which exhibit an opposite sign of AHE loops. Thus, the elevated temperature alters the dominant magnetization from Tb sublattice to Fe sublattice, which causes such an anomalous behavior. To show the influence of Joule heating on compensated magnetisms, the AHE measurements under different electrical currents are performed for Pt/$Fe_{0.68}Tb_{0.32}$/Ta multilayers. Following the increased current densities, a sign reversal of the AHE loops can be observed at large electrical density as shown in Fig. S6 of the Supplemental Material [34].

The evolution of critical switching current density (J_C^{th}) as a function of H_x is summarized in Figs. 4(a) and 4(b), in which stable SOT switching is evident for the Fe-dominated and Tb-dominated samples, respectively. The amplitude of J_C^{th} reduces with increased H_x, which occurs as a result of the reduced energy barrier [27–29]. Specifically, the magnetization orientation of Fe sublattices in the Fe-dominated (Tb-dominated) samples is switched from the down state (up state) to the up state (down state) under the positive H_x and positive J_C, respectively. A variation of J_C^{th} with Tb concentration (x) together with a maximized J_C^{th} at $x_c = 0.25$ are observed, as shown in Fig. 4(c). A further increase of Tb concentration (x) above x_c leads to a decreased J_C^{th}.

To quantify the SOT efficiency, harmonic Hall voltage measurements are carried out [46–50]. The dampinglike effective fields (H_{DL}) can be determined by sweeping H_x [28,29]. Figures 5(a) and 5(b) [5(c) and 5(d)] correspond to the first-harmonic $V_{1\omega}$ and second-harmonic $V_{2\omega}$ signals as a function of H_x for the Fe-dominated $Fe_{0.80}Tb_{0.20}$ [Tb-dominated $Fe_{0.65}Tb_{0.35}$] samples at $J_C = 0.3 \times 10^7$ A cm^{-2}, respectively. In particular, H_{DL} can be calculated:

$$H_{\text{DL}} \approx -2\frac{\partial V_{2\omega}}{\partial H_x}\Big/\frac{\partial^2 V_{1\omega}}{\partial H_x^2}. \tag{1}$$

For the upward (net) magnetization states [brown curves in Figs. 5(a)–5(d)], both reversed $V_{1\omega}$ and $V_{2\omega}$ signals can be observed, implying the same sign of H_{DL} for both the Fe-dominated and the Tb-dominated samples. Since the PHE resistance (R_{PHE}) is much smaller than the AHE

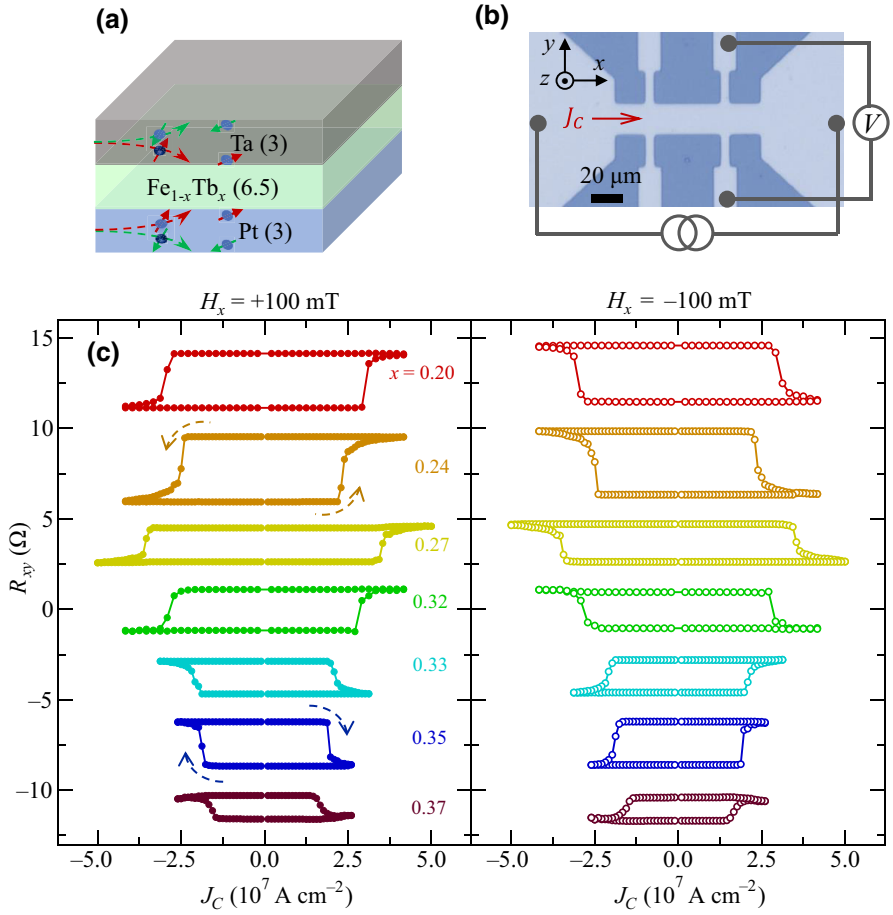

FIG. 3. (a) Schematic illustration of SOT switching in $Pt/Fe_{1-x}Tb_x/Ta$ multilayers. The red and green arrows correspond to the orientation of spin polarizations. (b) An optical image of the Hall bar devices and the measurement configuration. (c) The current-induced SOT switching under opposite in-plane fields of $H_x = \pm 100$ mT for samples with various Tb concentrations (x). The dashed arrows depict the switching polarities.

resistance (R_{xy}) in $Fe_{1-x}Tb_x$ films ($R_{PHE}/R_{xy} \approx 0.05$), the contribution from R_{PHE} is neglected. In addition, the temperature rise from Joule heating and the resulting anomalous Nernst effect are estimated in part 6 and part 7 of the Supplemental Material, respectively [34].

The dependence of H_{DL} on the current density J_C is summarized in Fig. 5(e). Through a linear fitting, the SOT efficiency χ_{SOT} ($\chi_{SOT} = H_{DL}/J_C$) for $Fe_{0.80}Tb_{0.20}$ and $Fe_{0.65}Tb_{0.35}$ samples is determined to be 1.10×10^{-6} and 0.95×10^{-6} mT cm^2 A^{-1}, respectively. To precisely

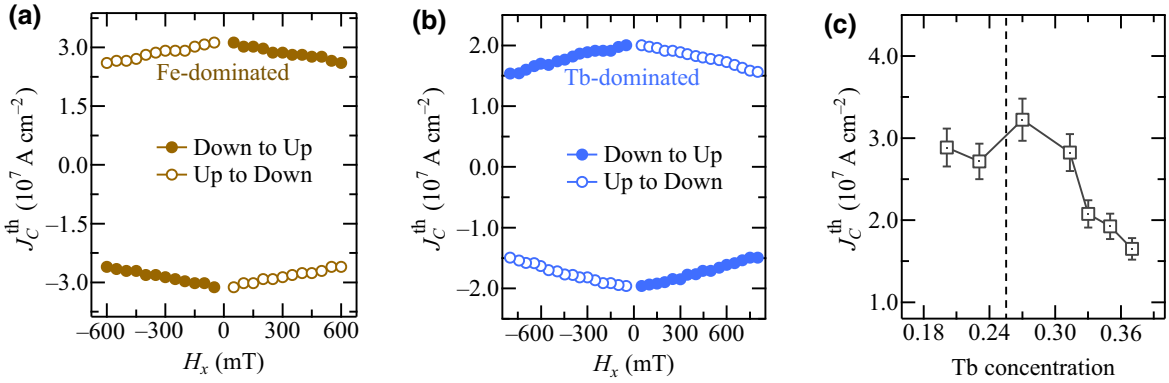

FIG. 4. The switching phase diagram for Fe-dominated $Fe_{0.80}Tb_{0.20}$ (a) and Tb-dominated $Fe_{0.65}Tb_{0.35}$ (b). The critical switching current densities (J_C^{th}) are acquired under various in-plane fields H_x. (c) The dependence of J_C^{th} as a function of Tb concentration (x).

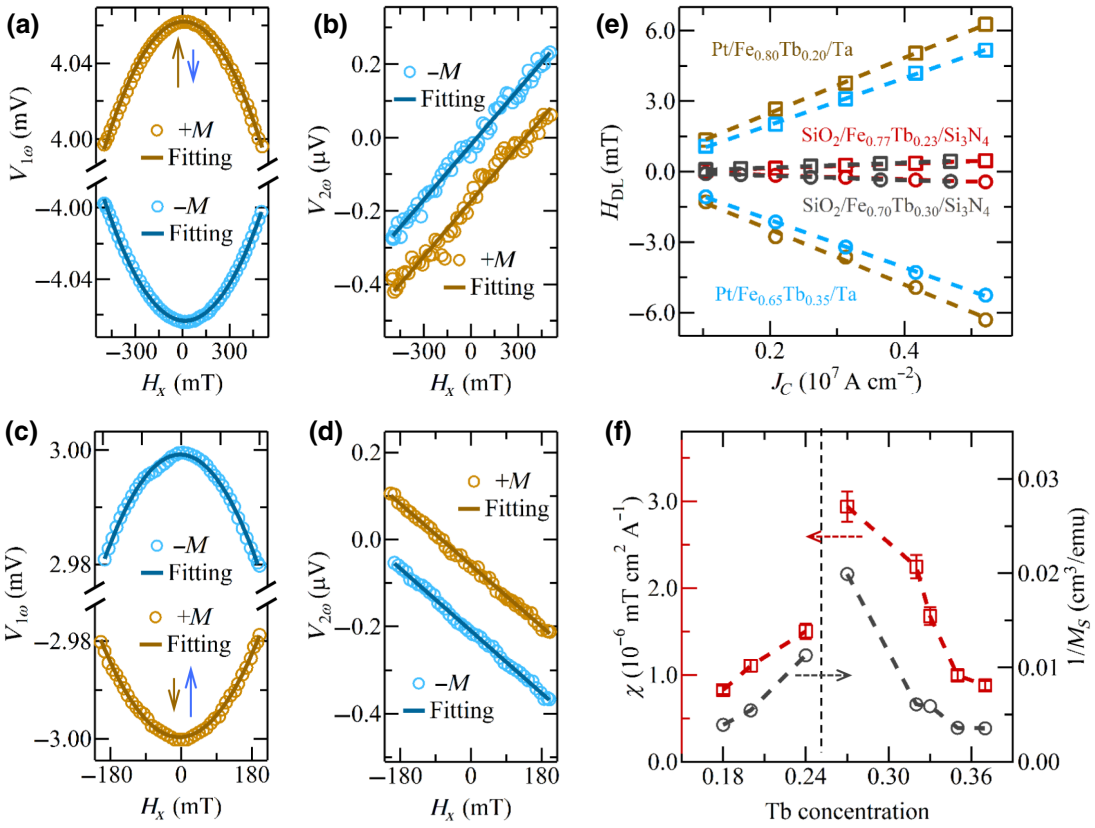

FIG. 5. (a) The first-harmonic $V_{1\omega}$ and (b) second-harmonic $V_{2\omega}$ Hall signals as a function of longitudinal in-plane field (H_x) for the Fe-dominated $Fe_{0.80}Tb_{0.20}$ sample. (c) The first-harmonic $V_{1\omega}$ and (d) second-harmonic $V_{2\omega}$ Hall signals as a function of H_x for the Tb-dominated $Fe_{0.65}Tb_{0.35}$ sample. (e) The dependence of dampinglike effective field H_{DL} on the current density J_C for $Pt/Fe_{1-x}Tb_x/Ta$ and $SiO_2/Fe_{1-x}Tb_x/Si_3N_4$ samples. (f) The evolution of SOT efficiency χ_{SOT} (left panel) and the inverse magnetization $1/M_S$ (right panel) as a function of Tb concentration (x). The brown and blue arrows denote the magnetization orientations of Fe and Tb sublattices, respectively.

identify the contribution from bulk self-torque in $Fe_{1-x}Tb_x$ single layers, harmonic Hall voltage measurements are also conducted for $SiO_2/Fe_{1-x}Tb_x/Si_3N_4$. Compared with the SOT generated in $Pt/Fe_{1-x}Tb_x/Ta$ multilayers, the bulk self-torque in various $Fe_{1-x}Tb_x$ single layers is negligible, as shown in Fig. 5(e). Figure 5(f) shows the evolution of χ_{SOT} as a function of the Tb concentration (x) for $Pt/Fe_{1-x}Tb_x/Ta$. Upon approaching x_c, χ_{SOT} can reach 3.0×10^{-6} mT cm^2 A^{-1}. Note that a similar trend for χ_{SOT} vs $1/M_s$ can also be identified in the right-hand panel of Fig. 5(f). This is due to the fact that the SOT efficiency ($\chi_{SOT} \approx H_{DL}/J_C \approx \hbar\theta_{sh}^{eff}/2eM_st$) is inversely proportional to M_S, with $\hbar$, θ_{sh}^{eff}, and t being the reduced Planck constant, the spin Hall angle, and the thickness of magnetic layer, respectively [28,29]. Since M_S exhibits a minimum value at x_c, the enhanced SOT efficiency χ_{SOT} can be attributed to the reduction of M_S, as suggested by earlier studies [9,10,12].

The evolution of the effective spin Hall angle (θ_{sh}^{eff}) is also calculated, as shown in Fig. S10 of the Supplemental Material [34]. A value of $\theta_{sh}^{eff} \sim 0.35$ and a slight reduction around x_c are observed. Notably, the nearly same values of θ_{sh}^{eff} crossing x_c are also reported in similar compensated FIMs [51,52]. Meanwhile, Zhu *et al.* reported a reduction of θ_{sh}^{eff} in $Pt_{0.75}Ti_{0.25}$(5.6 nm)/$Fe_{1-x}Tb_x$(8 nm) bilayers upon approaching x_c [44], which is attributed to the reduced rate of spin transfer to the magnetization, as compared with the rate of spin relaxation. This could likely explain the results of our experiments.

A larger critical switching current density J_C^{th} close to x_c is observed, as shown in Fig. 4(c). When approaching x_c, the enhancement of anisotropy field H_K (approximately 7 times) is stronger than that of χ_{SOT} (approximately 3 times). Based on the macrospin model [53,54], the contributing factors of J_C^{th} are given by

$$J_C^{th} = \frac{2e}{\hbar}\frac{M_S t}{\theta_{sh}^{eff}}\left(\frac{H_K}{2} - \frac{H_x}{\sqrt{2}}\right), \tag{2}$$

where the in-plane field (H_x) is much smaller than H_K. According to the measured χ_{SOT}, J_C^{th} can be estimated by H_K/χ_{SOT}. The enhanced J_C^{th} can be attributed to the substantially increased H_K, when approaching x_c. With Tb concentration (x) being varied from x_c, H_K is reduced

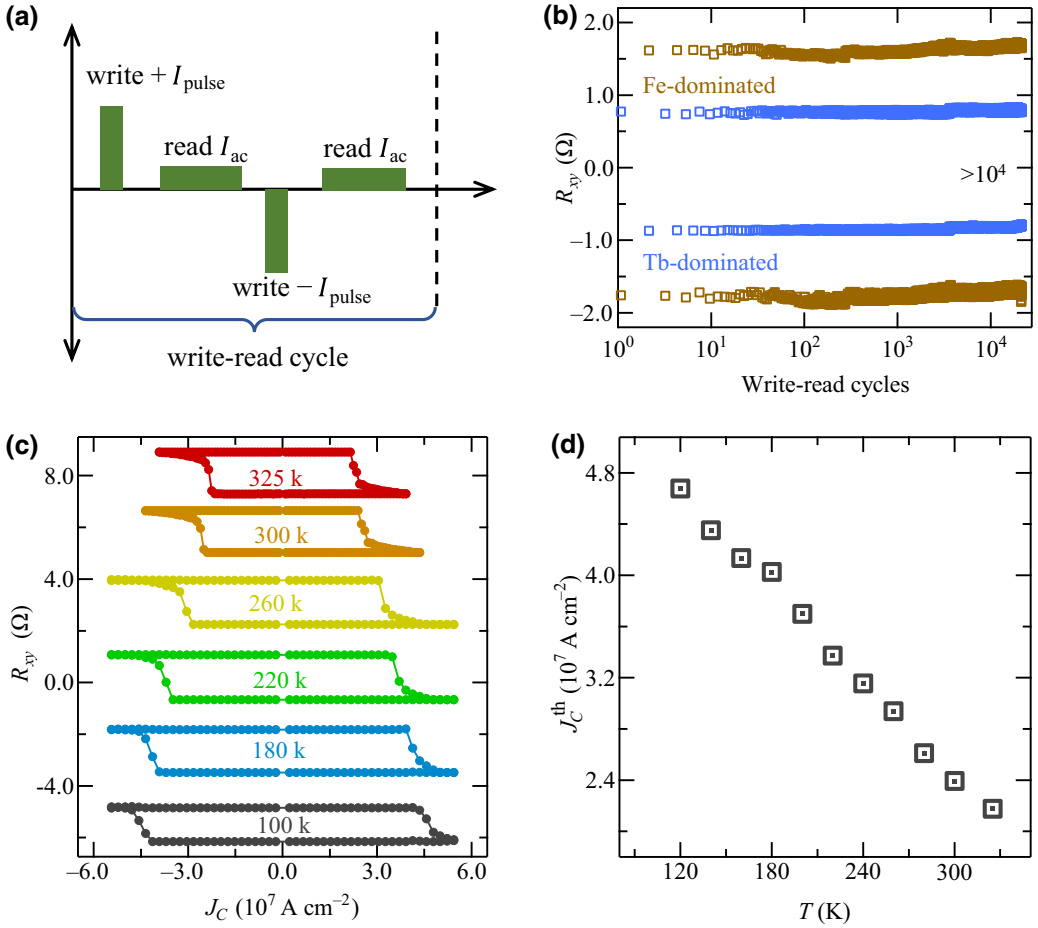

FIG. 6. (a) Measurement method for endurance test. We apply a small ac current to probe the AHE resistance R_{xy} after applying either positive ($+I_{pulse}$) or negative ($-I_{pulse}$) current pulses. (b) Endurance results with $> 10^4$ write-read cycles for the Fe-dominated and the Tb-dominated samples. (c) Under $H_x = +100$ mT, current-induced SOT switching measurements for $Fe_{0.68}Tb_{0.32}$ sample, which are performed over a wide temperature range (100–325 K). (d) The evolution of critical switching current density (J_C^{th}) as a function of temperature.

and J_C^{th} decreases with a further increase of Tb concentration (x), as shown in Fig. 4(c). Note that J_C^{th} based on the macrospin model could be overestimated due to the presence of multidomain structures in micrometer-sized samples [55].

C. Endurance test and temperature dependence

Stability is of vital importance for practical applications of SOT devices. An endurance test of the Fe-dominated and the Tb-dominated samples is conducted. During this test, we first apply a positive writing pulse ($+I_{pulse}$) of 2 ms in width and then record the corresponding AHE resistance (R_{xy}) with a small ac sensing current ($I_{ac} = 0.5$ mA). A negative writing current pulse ($-I_{pulse}$) is subsequently applied, and the corresponding values of R_{xy} are recorded, as shown in Fig. 6(a). Figure 6(b) shows the time trace of R_{xy} for $> 10^4$ "write + read" processes. Nearly the same level of R_{xy} (degradation <3%) after applying $>10^4$ current pulses (lasting for 24 hours) is observed, which demonstrates a good stability of the Fe-Tb-based SOT devices. Meanwhile, SOT switching is repeated on the same devices for over 10^4 cycles, which witnesses nearly the same level of R_{xy}, as shown in part 9 of the Supplemental Material [34].

Magnetic properties of the RE-TM FIMs are reported to be sensitive to environmental temperature, since the magnetization of the RE and TM sublattices exhibits different temperature dependency. Note that the magnetization compensation temperature (T_M) can be found well below and above 300 K for the Fe-dominated and Tb-dominated samples, which can be found in part 10 of the Supplemental Material [34]. We consequently examine the temperature-dependent SOT switching in $Pt/Fe_{0.65}Tb_{0.35}/Ta$ (Tb-dominated) multilayers. In the temperature range between 100 and 325 K, a deterministic SOT switching can be consistently obtained, as shown in Fig. 6(c). The increased J_C^{th} with decreased temperature can be due to the

enhancement of both the magnetic anisotropy and the net saturation magnetization with the decreased temperature, as shown in Fig. 6(d).

IV. CONCLUSIONS

In summary, $Fe_{1-x}Tb_x$ ferrimagnetic films of varied Tb concentrations (x), and of a fixed thickness 6.5 nm, are fabricated. The compensated magnetism in $Fe_{1-x}Tb_x$ alloys is studied through magnetometry and anomalous Hall effect measurements, which are verified via XMCD measurements. The compositional compensation point can be determined to be $x_c = 0.25$. Subsequently, current-induced SOTs are employed to manipulate the magnetization vectors in $Pt/Fe_{1-x}Tb_x/Ta$ multilayers. The SOT efficiency χ_{SOT} is significantly enhanced near $x_c = 0.25$ and can reach 3.0×10^{-6} mT cm^2 A^{-1}, which occurs as a result of the reduced net magnetization M_S at the compensated point. The endurance test demonstrates a good stability of $Fe_{1-x}Tb_x$-based SOT devices. Since $Fe_{1-x}Tb_x$ exhibits a much larger magnetic anisotropy than standard ferromagnets such as Co and Co-Fe-B, or ferrimagnets such as Co-Gd and Gd-Fe-Co, our results suggest that Fe-Tb could serve as another promising building block for scaling down spintronic devices, while maintaining a high thermal stability.

ACKNOWLEDGMENTS

Work carried out at Tsinghua is supported by the National Natural Science Foundation of China (Grant Nos. 52271181 and 51831005), the National Key R&D Program of China (Grant No. 2022YFA14052100), the NSF Distinguished Young Scholars Grant (No. 12225409), Beijing Natural Science Foundation (Grant No. Z190009), and the Beijing Advanced Innovation Center for Future Chip (ICFC).

[1] J. Finley and L. Liu, Spintronics with compensated ferrimagnets, Appl. Phys. Lett. **116**, 110501 (2020).
[2] H.-A. Zhou, T. Xu, H. Bai, and W. Jiang, Efficient spintronics with fully compensated ferrimagnets, J. Phys. Soc. Jpn. **90**, 081006 (2021).
[3] S. K. Kim, G. S. D. Beach, K.-J. Lee, T. Ono, T. Rasing, and H. Yang, Ferrimagnetic spintronics, Nat. Mater. **21**, 24 (2022).
[4] S. K. Kim, Fast and efficient switching with ferrimagnets, Nat. Electron. **3**, 18 (2020).
[5] Y. Zhang, X. Feng, Z. Zheng, Z. Zhang, K. Lin, X. Sun, G. Wang, J. Wang, J. Wei, P. Vallobra, Y. He, Z. Wang, L. Chen, K. Zhang, Y. Xu, and W. Zhao, Ferrimagnets for spintronic devices: From materials to applications, Appl. Phys. Rev. **10**, 011301 (2023).
[6] C. D. Stanciu, A. V. Kimel, F. Hansteen, A. Tsukamoto, A. Itoh, A. Kirilyuk, and T. Rasing, Ultrafast spin dynamics across compensation points in ferrimagnetic GdFeCo: The role of angular momentum compensation, Phys. Rev. B **73**, 220402 (2006).
[7] I. Radu, K. Vahaplar, C. Stamm, T. Kachel, N. Pontius, H. A. Dürr, T. A. Ostler, J. Barker, R. F. L. Evans, R. W. Chantrell, A. Tsukamoto, A. Itoh, A. Kirilyuk, T. Rasing, and A. V. Kimel, Transient ferromagnetic-like state mediating ultrafast reversal of antiferromagnetically coupled spins, Nature **472**, 205 (2011).
[8] J. Becker, A. Tsukamoto, A. Kirilyuk, J. C. Maan, T. Rasing, P. C. M. Christianen, and A. V. Kimel, Ultrafast Magnetism of a Ferrimagnet across the Spin-Flop Transition in High Magnetic Fields, Phys. Rev. Lett. **118**, 117203 (2017).
[9] J. Finley and L. Liu, Spin-Orbit-Torque Efficiency in Compensated Ferrimagnetic Cobalt-Terbium Alloys, Phys. Rev. Appl. **6**, 054001 (2016).
[10] R. Mishra, J. Yu, X. Qiu, M. Motapothula, T. Venkatesan, and H. Yang, Anomalous Current-Induced Spin Torques in Ferrimagnets near Compensation, Phys. Rev. Lett. **118**, 167201 (2017).
[11] S.-G. Je, J.-C. Rojas-Sánchez, T. H. Pham, P. Vallobra, G. Malinowski, D. Lacour, T. Fache, M.-C. Cyrille, D.-Y. Kim, S.-B. Choe, M. Belmeguenai, M. Hehn, S. Mangin, G. Gaudin, and O. Boulle, Spin-orbit torque-induced switching in ferrimagnetic alloys: Experiments and modeling, Appl. Phys. Lett. **112**, 062401 (2018).
[12] H. Wu, Y. Xu, P. Deng, Q. Pan, S. A. Razavi, K. Wong, L. Huang, B. Dai, Q. Shao, G. Yu, X. Han, J.-C. Rojas-Sánchez, S. Mangin, and K. L. Wang, Spin-orbit torque switching of a nearly compensated ferrimagnet by topological surface states, Adv. Mater. **31**, 1901681 (2019).
[13] Y. Mimura and N. Imamura, Magnetic properties of amorphous Tb-Fe thin films prepared by rf sputtering, Appl. Phys. Lett. **28**, 746 (1976).
[14] P. Hansen, C. Clausen, G. Much, M. Rosenkranz, and K. Witter, Magnetic and magneto-optical properties of rare-earth transition-metal alloys containing Gd, Tb, Fe, Co, J. Appl. Phys. **66**, 756 (1989).
[15] B. Hebler, A. Hassdenteufel, P. Reinhardt, H. Karl, and M. Albrecht, Ferrimagnetic Tb–Fe alloy thin films: Composition and thickness dependence of magnetic properties and all-optical switching, Front. Mater. **3**, 8 (2016).
[16] K. Cai, Z. Zhu, J. M. Lee, R. Mishra, L. Ren, S. D. Pollard, P. He, G. Liang, K. L. Teo, and H. Yang, Ultrafast and energy-efficient spin–orbit torque switching in compensated ferrimagnets, Nat. Electron. **3**, 37 (2020).
[17] K.-J. Kim, S. K. Kim, Y. Hirata, S.-H. Oh, T. Tono, D.-H. Kim, T. Okuno, W. S. Ham, S. Kim, G. Go, Y. Tserkovnyak, A. Tsukamoto, T. Moriyama, K.-J. Lee, and T. Ono, Fast domain wall motion in the vicinity of the angular momentum compensation temperature of ferrimagnets, Nat. Mater. **16**, 1187 (2017).
[18] L. Caretta, M. Mann, F. Büttner, K. Ueda, B. Pfau, C. M. Günther, P. Hessing, A. Churikova, C. Klose, M. Schneider, D. Engel, C. Marcus, D. Bono, K. Bagschik, S. Eisebitt, and G. S. D. Beach, Fast current-driven domain walls and small skyrmions in a compensated ferrimagnet, Nat. Nanotechnol. **13**, 1154 (2018).
[19] S. Vélez, J. Schaab, M. S. Wörnle, M. Müller, E. Gradauskaite, P. Welter, C. Gutgsell, C. Nistor, C. L.

Degen, M. Trassin, M. Fiebig, and P. Gambardella, High-speed domain wall racetracks in a magnetic insulator, Nat. Commun. **10**, 4750 (2019).

[20] C. O. Avci, E. Rosenberg, L. Caretta, F. Büttner, M. Mann, C. Marcus, D. Bono, C. A. Ross, and G. S. D. Beach, Interface-driven chiral magnetism and current-driven domain walls in insulating magnetic garnets, Nat. Nanotechnol. **14**, 561 (2019).

[21] L. Caretta, S.-H. Oh, T. Fakhrul, D.-K. Lee, B. H. Lee, S. K. Kim, C. A. Ross, K.-J. Lee, and G. S. D. Beach, Relativistic kinematics of a magnetic soliton, Science **370**, 1438 (2020).

[22] S. Woo, K. M. Song, X. Zhang, Y. Zhou, M. Ezawa, X. Liu, S. Finizio, J. Raabe, N. J. Lee, S.-I. Kim, S.-Y. Park, Y. Kim, J.-Y. Kim, D. Lee, O. Lee, J. W. Choi, B.-C. Min, H. C. Koo, and J. Chang, Current-driven dynamics and inhibition of the skyrmion Hall effect of ferrimagnetic skyrmions in GdFeCo films, Nat. Commun. **9**, 959 (2018).

[23] S. Woo, K. M. Song, X. Zhang, M. Ezawa, Y. Zhou, X. Liu, M. Weigand, S. Finizio, J. Raabe, M.-C. Park, K.-Y. Lee, J. W. Choi, B.-C. Min, H. C. Koo, and J. Chang, Deterministic creation and deletion of a single magnetic skyrmion observed by direct time-resolved X-ray microscopy, Nat. Electron. **1**, 288 (2018).

[24] Y. Hirata, D.-H. Kim, S. K. Kim, D.-K. Lee, S.-H. Oh, D.-Y. Kim, T. Nishimura, T. Okuno, Y. Futakawa, H. Yoshikawa, A. Tsukamoto, Y. Tserkovnyak, Y. Shiota, T. Moriyama, S.-B. Choe, K.-J. Lee, and T. Ono, Vanishing skyrmion Hall effect at the angular momentum compensation temperature of a ferrimagnet, Nat. Nanotechnol. **14**, 232 (2019).

[25] T. Xu, Z. Chen, H.-A. Zhou, Z. Wang, Y. Dong, L. Aballe, M. Foerster, P. Gargiani, M. Valvidares, D. M. Bracher, T. Savchenko, A. Kleibert, R. Tomasello, G. Finocchio, S.-G. Je, M.-Y. Im, D. A. Muller, and W. Jiang, Imaging the spin chirality of ferrimagnetic Neel skyrmions stabilized on topological antiferromagnetic Mn_3Sn, Phys. Rev. Mater. **5**, 084406 (2021).

[26] I. Mihai Miron, G. Gaudin, S. Auffret, B. Rodmacq, A. Schuhl, S. Pizzini, J. Vogel, and P. Gambardella, Current-driven spin torque induced by the Rashba effect in a ferromagnetic metal layer, Nat. Mater. **9**, 230 (2010).

[27] I. M. Miron, K. Garello, G. Gaudin, P.-J. Zermatten, M. V. Costache, S. Auffret, S. Bandiera, B. Rodmacq, A. Schuhl, and P. Gambardella, Perpendicular switching of a single ferromagnetic layer induced by in-plane current injection, Nature **476**, 189 (2011).

[28] L. Liu, O. J. Lee, T. J. Gudmundsen, D. C. Ralph, and R. A. Buhrman, Current-Induced Switching of Perpendicularly Magnetized Magnetic Layers Using Spin Torque from the Spin Hall Effect, Phys. Rev. Lett. **109**, 096602 (2012).

[29] L. Liu, C.-F. Pai, Y. Li, H. W. Tseng, D. C. Ralph, and R. A. Buhrman, Spin-torque switching with the giant spin Hall effect of tantalum, Science **336**, 555 (2012).

[30] A. Manchon, J. Železný, I. M. Miron, T. Jungwirth, J. Sinova, A. Thiaville, K. Garello, and P. Gambardella, Current-induced spin-orbit torques in ferromagnetic and antiferromagnetic systems, Rev. Mod. Phys. **91**, 035004 (2019).

[31] A. Tang, T. Xu, S. Liu, Y. Liang, H. Chen, D. Yan, Y. Shi, P. Yu, R. Yu, Y. Lin, T. Nan, W. Jiang, and D. Yi, Implementing complex oxides for efficient room-temperature spin–orbit torque switching, Adv. Electron. Mater. **8**, 2200514 (2022).

[32] Q. Liu, L. Zhu, X. S. Zhang, D. A. Muller, and D. C. Ralph, Giant bulk spin–orbit torque and efficient electrical switching in single ferrimagnetic FeTb layers with strong perpendicular magnetic anisotropy, Appl. Phys. Rev. **9**, 021402 (2022).

[33] A. Barla, J. Nicolás, D. Cocco, S. M. Valvidares, J. Herrero-Martin, P. Gargiani, J. Moldes, C. Ruget, E. Pellegrin, and S. Ferrer, Design and performance of BOREAS, the beamline for resonant X-ray absorption and scattering experiments at the ALBA synchrotron light source, J. Synchrotron Rad. **23**, 1507 (2016).

[34] See Supplementary Material at http://link.aps.org/supplemental/10.1103/PhysRevApplied.19.034088 for additional information on determination of perpendicular magnetic anisotropy fields, current-induced SOT switching measurements in inverted multilayers and control sample, temperature rise due to Joule heating effect, thermal electric contribution, effective spin Hall angle, endurance test, and magnetization compensation temperature.

[35] Z. Zheng, Y. Zhang, V. Lopez-Dominguez, L. Sánchez-Tejerina, J. Shi, X. Feng, L. Chen, Z. Wang, Z. Zhang, K. Zhang, B. Hong, Y. Xu, Y. Zhang, M. Carpentieri, A. Fert, G. Finocchio, W. Zhao, and P. Khalili Amiri, Field-free spin-orbit torque-induced switching of perpendicular magnetization in a ferrimagnetic layer with a vertical composition gradient, Nat. Commun. **12**, 4555 (2021).

[36] T. Shirakawa, Y. Nakajima, K. Okamoto, S. Matsushita, and Y. Sakurai, The Kerr and the Hall effects in amorphous magnetic films, AIP Conf. Proc. **34**, 349 (1976).

[37] Y. Mimura, N. Imamura, and Y. Kushiro, Hall effect in rare-earth–transition-metal amorphous alloy films, J. Appl. Phys. **47**, 3371 (1976).

[38] R. Malmhäll, Extraordinary Hall resistivity in amorphous terbium–iron thin films and its temperature dependence, J. Appl. Phys. **54**, 5128 (1983).

[39] S. Woo, M. Mann, A. J. Tan, L. Caretta, and G. S. D. Beach, Enhanced spin-orbit torques in Pt/Co/Ta heterostructures, Appl. Phys. Lett. **105**, 212404 (2014).

[40] J. Yu, X. Qiu, Y. Wu, J. Yoon, P. Deorani, J. M. Besbas, A. Manchon, and H. Yang, Spin orbit torques and Dzyaloshinskii-Moriya interaction in dual-interfaced Co-Ni multilayers, Sci. Rep. **6**, 32629 (2016).

[41] J. W. Lee, J. Y. Park, J. M. Yuk, and B.-G. Park, Spin-Orbit Torque in a Perpendicularly Magnetized Ferrimagnetic CoTb Single Layer, Phys. Rev. Appl. **13**, 044030 (2020).

[42] R. Q. Zhang, *et al.*, Current-induced magnetization switching in a CoTb amorphous single layer, Phys. Rev. B **101**, 214418 (2020).

[43] S. Krishnia, E. Haltz, L. Berges, L. Aballe, M. Foerster, L. Bocher, R. Weil, A. Thiaville, J. Sampaio, and A. Mougin, Spin-Orbit Coupling in Single-Layer Ferrimagnets: Direct Observation of Spin-Orbit Torques and Chiral Spin Textures, Phys. Rev. Appl. **16**, 024040 (2021).

[44] L. Zhu and D. C. Ralph, Strong variation of spin-orbit torque with relative spin relaxation rates in ferrimagnets, arXiv:2210.11042.

[45] T. H. Pham, S. G. Je, P. Vallobra, T. Fache, D. Lacour, G. Malinowski, M. C. Cyrille, G. Gaudin, O. Boulle, M. Hehn, J. C. Rojas-Sánchez, and S. Mangin, Thermal Contribution to the Spin-Orbit Torque in Metallic-Ferrimagnetic Systems, Phys. Rev. Appl. **9**, 064032 (2018).

[46] J. Kim, J. Sinha, M. Hayashi, M. Yamanouchi, S. Fukami, T. Suzuki, S. Mitani, and H. Ohno, Layer thickness dependence of the current-induced effective field vector in Ta|CoFeB|MgO, Nat. Mater. **12**, 240 (2013).

[47] M. Hayashi, J. Kim, M. Yamanouchi, and H. Ohno, Quantitative characterization of the spin-orbit torque using harmonic Hall voltage measurements, Phys. Rev. B **89**, 144425 (2014).

[48] K. Garello, I. M. Miron, C. O. Avci, F. Freimuth, Y. Mokrousov, S. Blügel, S. Auffret, O. Boulle, G. Gaudin, and P. Gambardella, Symmetry and magnitude of spin–orbit torques in ferromagnetic heterostructures, Nat. Nanotechnol. **8**, 587 (2013).

[49] C. O. Avci, K. Garello, M. Gabureac, A. Ghosh, A. Fuhrer, S. F. Alvarado, and P. Gambardella, Interplay of spin-orbit torque and thermoelectric effects in ferromagnet/normal-metal bilayers, Phys. Rev. B **90**, 224427 (2014).

[50] H. Yang, H. Chen, M. Tang, S. Hu, and X. Qiu, Characterization of spin-orbit torque and thermoelectric effects via coherent magnetization rotation, Phys. Rev. B **102**, 024427 (2020).

[51] W. Seung Ham, S. Kim, D.-H. Kim, K.-J. Kim, T. Okuno, H. Yoshikawa, A. Tsukamoto, T. Moriyama, and T. Ono, Temperature dependence of spin-orbit effective fields in Pt/GdFeCo bilayers, Appl. Phys. Lett. **110**, 242405 (2017).

[52] K. Ueda, M. Mann, P. W. P. de Brouwer, D. Bono, and G. S. D. Beach, Temperature dependence of spin-orbit torques across the magnetic compensation point in a ferrimagnetic TbCo alloy film, Phys. Rev. B **96**, 064410 (2017).

[53] K.-S. Lee, S.-W. Lee, B.-C. Min, and K.-J. Lee, Threshold current for switching of a perpendicular magnetic layer induced by spin Hall effect, Appl. Phys. Lett. **102**, 112410 (2013).

[54] S. Fukami, T. Anekawa, C. Zhang, and H. Ohno, A spin–orbit torque switching scheme with collinear magnetic easy axis and current configuration, Nat. Nanotechnol. **11**, 621 (2016).

[55] L. Zhu, D. C. Ralph, and R. A. Buhrman, Lack of Simple Correlation between Switching Current Density and Spin-Orbit-Torque Efficiency of Perpendicularly Magnetized Spin-Current-Generator–Ferromagnet Heterostructures, Phys. Rev. Appl. **15**, 024059 (2021).